

AnomalyNCD: Towards Novel Anomaly Class Discovery in Industrial Scenarios

Ziming Huang*, Xurui Li*, Haotian Liu*, Feng Xue, Member, IEEE, Yuzhe Wang, and Yu Zhou Member, IEEE.
<https://github.com/HUST-SLOW/AnomalyNCD>

Abstract—In the industrial scenario, anomaly detection could locate but cannot classify anomalies. To complete their capability, we study to automatically discover and recognize visual classes of industrial anomalies. In terms of multi-class anomaly classification, previous methods cluster anomalies represented by frozen pre-trained models but often fail due to poor discrimination. Novel class discovery (NCD) has the potential to tackle this. However, it struggles with non-prominent and semantically weak anomalies that challenge network learning focus. To address these, we introduce AnomalyNCD, a multi-class anomaly classification framework compatible with existing anomaly detection methods. This framework learns anomaly-specific features and classifies anomalies in a self-supervised manner. Initially, a technique called Main Element Binarization (MEBin) is first designed, which segments primary anomaly regions into masks to alleviate the impact of incorrect detections on learning. Subsequently, we employ mask-guided contrastive representation learning to improve feature discrimination, which focuses network attention on isolated anomalous regions and reduces the confusion of erroneous inputs through re-corrected pseudo labels. Finally, to enable flexible classification at both region and image levels during inference, we develop a region merging strategy that determines the overall image category based on the classified anomaly regions. Our method outperforms the state-of-the-art works on the MVTec AD and MTD datasets. Compared with the current methods, AnomalyNCD combined with zero-shot anomaly detection method achieves a 10.8% F_1 gain, 8.8% NMI gain, and 9.5% ARI gain on MVTec AD, 12.8% F_1 gain, 5.7% NMI gain, and 10.8% ARI gain on MTD.

Index Terms—Multi-class anomaly classification, novel class discovery, binarization method, mask-guided attention, contrastive representation learning.

I. INTRODUCTION

IN recent years, industrial anomaly detection [1], [2], [3], [4] has garnered remarkable performance. It locates visual anomalies on the surface of industrial products but without recognizing fine-grained anomaly categories. For downstream anomaly treatments, it is necessary to recognize the anomaly classes, such as fracture, ablation, etc., and even discover novel anomaly categories that are constantly emerging. As human,

we can adeptly utilize visual knowledge to organize anomalies into homogeneous groups, even if the criteria for human classification is hard to summarize. However, machines cannot perform such multi-class anomaly classification satisfactorily without human supervision.

One available solution is anomaly clustering. Since the anomaly classes are highly related to the anomalies' appearance and their surrounding area, an intuitive way is to locate the anomalies and obtain the features of the anomalous region for clustering. As shown in Fig. 1 (a), Sohn *et al.* [5] proposed to cluster the anomalies' feature embeddings obtained from frozen networks using unsupervised clustering approaches, such as K-Means, hierarchical clustering, and Gaussian mixture models. Lee *et al.* [6] performed the feature reordering and selected the top- $k\%$ of patch embeddings of anomaly to be clustered. The solution works well when anomalies hold discriminative visual appearance. However, homogeneous anomaly patterns usually differ in shape, appearance, and location. Therefore, features extracted by frozen pre-trained networks are insufficient to distinguish different anomalies.

Another potential way for multi-class anomaly classification is to apply the novel class discovery (NCD) first proposed by Han *et al.* [7] in 2019, which learns representations of anomalies rather than using frozen networks. As shown in Fig. 1 (b), NCD methods separate these class-unknown samples into several clusters (i.e., **novel classes**) by conducting supervised learning (SL) in a set of samples with class annotation (i.e., **base classes**) and self-supervised learning (SSL) in all samples. However, NCD methods cannot be applied to industrial anomalies directly due to two obstructions: ① **Non-prominence**: The vanilla NCD assumed that subjects are centered in the images so that networks easily extract their semantics, while this assumption is not true in industrial scenarios. ② **Low-semantics**: In contrast to natural objects, industrial anomalies are typically less semantic, making the network hard to focus on anomalies but prone to background.

In this paper, we overcome both obstructions and provide a multi-class anomaly classification framework as a downstream module of existing anomaly detection methods, as illustrated in 1 (c). It learns to classify isolated anomalies, in which we guide the model's focus on real anomaly regions, rather than incorrect anomalies introduced by detection inevitably. Firstly, we propose a main element binarization (MEBin) method to extract main anomaly regions from anomaly detection results. It alleviates the negative impact of errors within detection results on the subsequent multi-class anomaly learning, which allows our method to be easily compatible with detection

* The first three authors contributed equally to this work.

This work was supported by the National Natural Science Foundation of China under Grant No.62176098. The computation is completed in the HPC Platform of Huazhong University of Science and Technology. (Corresponding author: Yu Zhou.)

Ziming Huang, Xurui Li, Haotian Liu, Yuzhe Wang, and Yu Zhou are with the School of Electronic Information and Communications, Huazhong University of Science and Technology, Wuhan 430074, China. (e-mail: zmhuang@hust.edu.cn; xrli_plus@hust.edu.cn; htliu_master@hust.edu.cn; yuzwang@hust.edu.cn; yuzhou@hust.edu.cn).

Feng Xue is with the School of Computer Science, University of Trento, Italy. (e-mail: feng.xue@unitn.it).

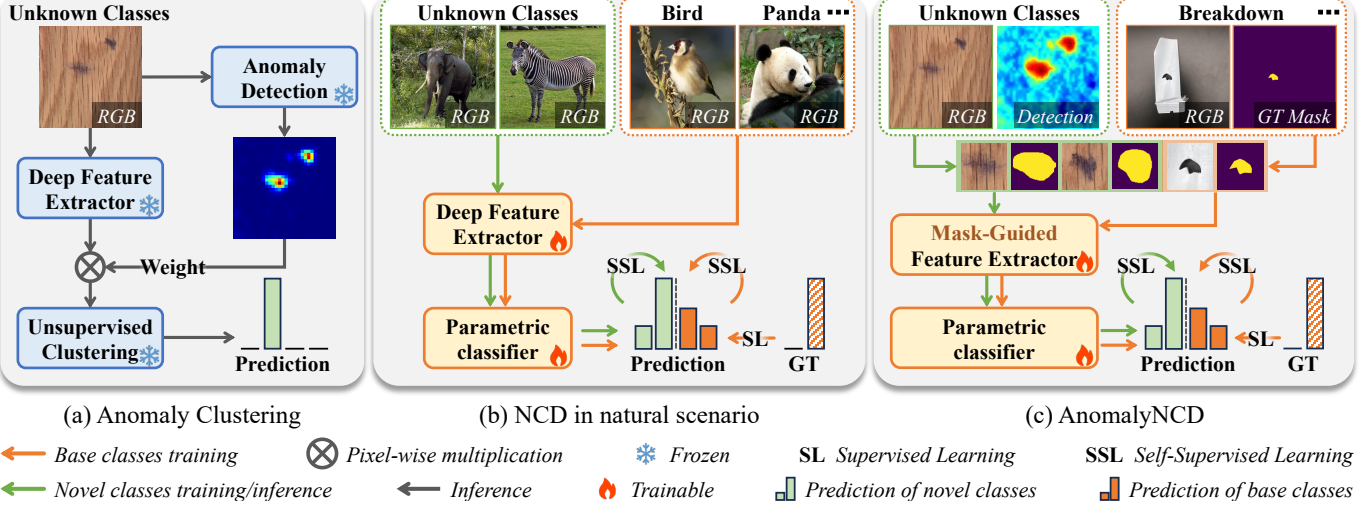


Fig. 1. **Comparison between solutions organizing anomalies into groups.** (a) Anomaly clustering methods employ unsupervised clustering algorithms to cluster the anomalies characterized by anomaly detection techniques and features extracted using pre-trained networks. (b) Vanilla NCD methods typically employ a trainable feature extractor and classifier. These components process object-centered images from both known and unknown classes. (c) Our method aims to learn feature of isolated anomaly region using anomaly-centered sub-images and masks from MEBin.

algorithms with varying precision. Secondly, we propose the mask-guided contrastive representation learning. It directs the network’s focus to individual anomaly region using anomaly masks from MEBin, so that our network learns discriminative features specific to anomalies and classifies each individual anomaly. Additionally, we use re-corrected pseudo labels in this learning method to prevent false-positive anomalies from training. Finally, to achieve more flexible classification in both region and image levels, we propose a region merging strategy, which determines the image category according to the classification of each region in the image. Experimental results on the MVTec AD [8] and MTD datasets [9] demonstrate the outstanding effectiveness of AnomalyNCD.

In summary, the major contributions of our work are:

- We apply NCD to industrial scenarios for the first time and propose a more effective framework than Anomaly Clustering, named AnomalyNCD. It can be seamlessly combined with anomaly detection methods and classify unseen anomalies detected into homogeneous groups.
- We deeply study the challenges in applying NCD to industrial scenarios, motivating us to propose MEBin and mask-guided contrastive representation learning for our network to focus on real anomalous regions and learn discriminative features of isolated anomalies.
- AnomalyNCD surpasses existing anomaly clustering methods and directly applied NCD methods on the MVTec AD and MTD datasets, providing a decent foundation for downstream anomaly treatments in industrial scenarios.

II. RELATED WORK

A. Deep Clustering and Its Application in Industrial Scenarios

Deep clustering methods such as IIC [10], GATCluster [11], SCAN [12], DERC [13], DSC [14], and SPICE [15] learn deep representation and clustering assignments simultaneously. However, the direct application cannot perform well

in multi-class anomaly classification. Therefore, two studies attempted to build deep clustering pipeline specific to fine-grained anomaly classes. Sohn *et al.* [5] proposed a simple but effective method to aggregate the patch features by anomaly map weighting. Uniformaly [6] only aggregates the patch features with the higher anomaly score to determine the classes. However, both of them use frozen model that cannot learn features specific to anomalies, especially for anomaly that are constantly emerging. Therefore, we adopt self-supervised learning to discover novel classes from unlabeled anomalies.

B. Novel Class Discovery

Novel Class Discovery setting was first formalized in [7]. It aims to cluster a set of unlabeled samples (**novel classes**), utilizing the knowledge transferred from labeled samples (**base classes**), where novel and base classes do not overlap. To tackle this problem, the early methods follows a two-stage pipeline [7], [16], [17]. The first stage is to learn representation from the base set to obtain prior knowledge for classification, which serves as the basis for the second one to train the model on the novel set. The methods in the first stage can be roughly divided into two categories: learning similarity function using labeled data [16], [17] and encoding features of labeled classes into latent representation [7]. More recent methods are one-stage [18], [19], [20]. By handling the base set and novel set simultaneously, one-stage methods extract better potential representations with less bias towards the base classes. Recently, NCD has been applied in several fields, such as medical image classification [21], [22]. In this paper, we leverage NCD in multi-class industrial anomaly classification for the first time, and propose mask-guided attention to direct the network’s focus on anomaly.

C. Representation Learning

Representation learning aims to extract meaningful visual representation for various tasks, such as object detection [23],

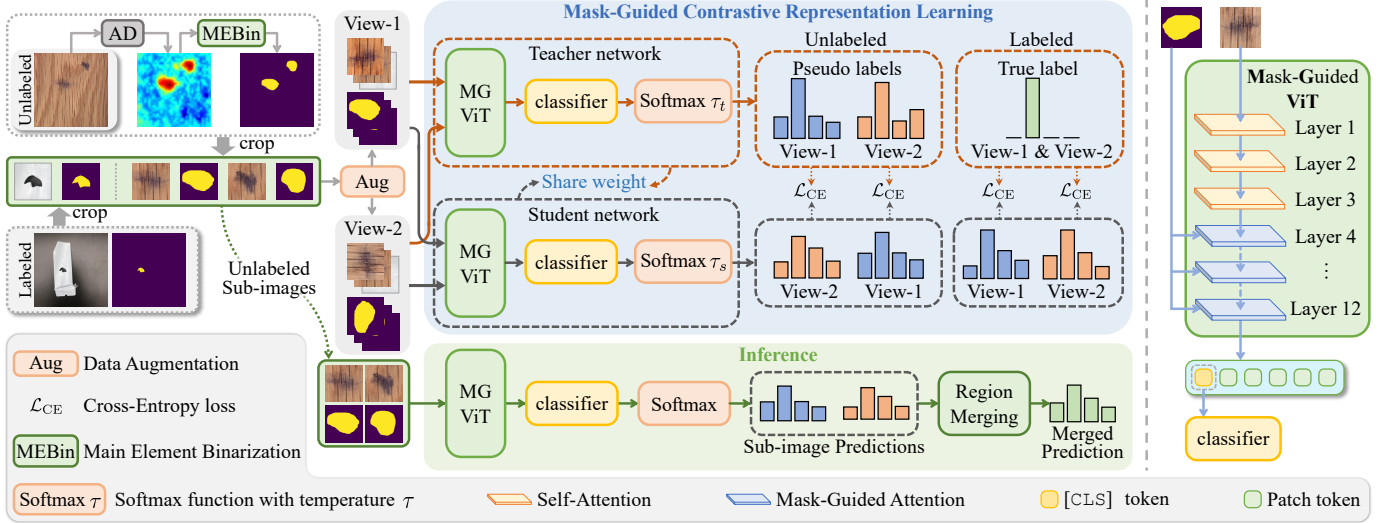


Fig. 2. **Illustration of Our AnomalyNCD Framework**, which contains three stages. First, we apply main element binarization (MEBin) to segment anomaly masks from the detection results and generate anomaly-centered sub-images. Second, for each sub-image, we generate two augmented views and feed them into the Vision Transformer (ViT) for self-supervised contrastive learning. During training, the anomaly masks guide the network to concentrate on the anomaly regions. During inference, we employ a region merging strategy to determine image category based on classified anomaly regions.

[24], [25], occlusion relationship reasoning [26], [27], [28], [29], and etc. The learning methods can be mainly divided into supervised one and unsupervised one. In unsupervised learning methods, contrastive learning is a powerful technique for learning discriminative representations. MoCo [30] and SimCLR [31] utilize positive and negative sample pairs with InfoNCE [32]. BYOL [33] and SimSiam [34] find that even without using negative samples, contrastive learning can achieve excellent performance. DINO [35] utilizes self-distillation without labels to train vision transformers, and self-supervised ViT features contain explicit information about the semantic segmentation of an image. We adopt the self-distillation [35], [36] technique to generate pseudo labels and leverage contrastive learning to learn the discriminative representations of the anomalies.

D. Binarization Approach

Binarization is one of the indispensable preprocessing steps for various vision tasks, e.g., segmentation [37], [38], [39], document image processing [40], [41], [42], medical image processing [43], [44], object detection [45], [46], [47], etc. Su *et al.* [48] proposes a document image binarization by using a combination of the local image contrast and the local image gradient. Roy *et al.* [44] develops an effective standard deviation approach to binarize gray MRI images. DiffuMask [49] employs a cross-attention map between text token and vision, then converts the probability map to a binary map through adaptive thresholding. To address pixels with a middle confidence score, it incorporates semantic affinity learning (i.e., AffinityNet [50]) to provide a refined estimation. However, aiming to precisely segment object boundary, the existing binarization methods may obtain trivial false positives and negatives. To avoid this, we design a main element binarization method to extract only the primary anomaly region in the

detection results, thereby reducing the impact of false positives and negatives on learning.

III. METHOD

The proposed AnomalyNCD aims to automatically discover and recognize the visual categories of industrial anomalies. Fig. 2 illustrates its overall framework. Preliminarily, we provide a formal and detailed definition of the NCD problem for industrial anomalies in Sec. III-A. The subsequent sections introduce AnomalyNCD comprehensively. In Sec. III-B, we outline the main element binarization method, which coarsely isolates anomalies to prevent both excessive and insufficient detections from disrupting the learning process. The anomalies are presented in anomaly-centered sub-images and corresponding masks. Then, in Sec. III-C, the mask-guided contrastive representation learning is introduced to learn discriminative features of anomalies under the guidance of the masks, so as to classify sub-images into various categories. Finally, beyond the region-level classification, we propose a region merging strategy in Sec. III-D to achieve robust image-level classification based on sub-image prediction.

A. Problem Definition

Given a set of unlabelled images $\mathcal{D}^u = \{I_i^u | i \in [1, N^u]\}$, the goal of AnomalyNCD is to assign them into \mathcal{C}^u classes (named “**Novel**” previously), where \mathcal{C}^u is known as a priori, referring to vanilla NCD [51], [52], [53]. To provide a better foundation for learning novel classes, we follow previous NCD tasks to assume a set of labeled anomaly images $\mathcal{D}^l = \{(I_i^l, y_i^l, M_i^l) | i \in [1, N^l]\}$ with \mathcal{C}^l classes available (named “**Base**” previously), where y_i^l is the one-hot class label, and M_i^l is the ground truth anomaly mask of image $I_i^l \in \mathcal{D}^l$. \mathcal{D}^l supplies the auxiliary knowledge of the industrial anomalies for grouping the images in \mathcal{D}^u . To study it more generally, we also perform experiments without \mathcal{D}^l in Sec. IV-C7.

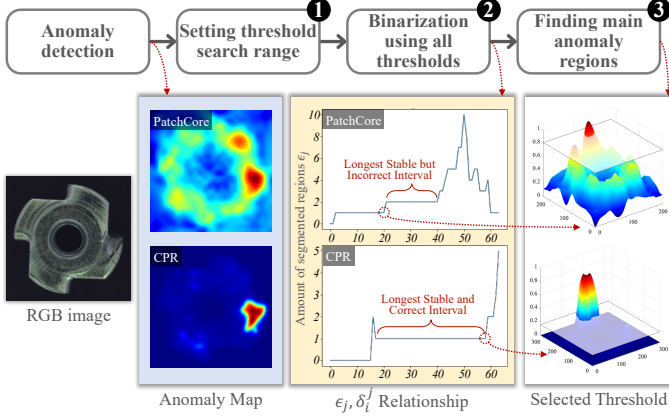


Fig. 3. **Pipeline of the Main Element Binarization Approach.** We visualize all steps using two anomaly detection methods, PatchCore [54] and CPR [55], for comparison. **Red** in the Anomaly Map indicates high probability, and **blue** indicates low probability.

B. Main Element Binarization for Unlabeled Anomaly Images

To provide a clear anomaly indication of unlabeled images, we use an anomaly detection method on I_i^u to generate an anomaly probability map, denoted as $A_i \in [0, 1]^{H \times W}$. However, perfect algorithms do not exist. A_i inevitably encounters false positives (over-detections) and false negatives (missed detections). These errors can negatively affect self-supervised multi-class anomaly classification. To alleviate these errors, we propose a Main Element Binarization (MEBin) approach to extract the principal structures of anomalous regions from A_i , minimizing trivial over-detections and missed detections.

Motivation: Since the primary anomalous regions remain consistent across small variations in threshold settings, our key idea involves determining a threshold range where the segmented areas demonstrate stability. Overall, the MEBin consists of three steps: ① Establishing a predefined range for threshold exploration; ② Binarizing A_i across all thresholds within this range; ③ Identifying the main elements in A_i based on the binarization results.

The first step is to set a reasonable search range $[s_{\min}, s_{\max}]$ for thresholds. To capture all potential anomalies across the set $\{A_i | i \in [1, N^u]\}$, the upper limit of this range, i.e., s_{\max} , is set to 1. Conversely, the lower limit, s_{\min} , is determined by the lowest anomaly score¹ found across the dataset, represented as $s_{\min} = \min(s_1, s_2, \dots, s_{N^u})$, where $s_i = \max(A_i)$. Such a lower limit helps minimize the likelihood of normal image pixels being segmented.

The second step is to binarize the anomaly map A_i using all thresholds in the range $[s_{\min}, s_{\max}]$, enabling the third step of analyzing segmented regions change with thresholds. Specifically, we uniformly sample \mathcal{T} thresholds in $[s_{\min}, s_{\max}]$, denoted as $\{\epsilon_j | j \in [1, \mathcal{T}]\}$. For each threshold ϵ_j , the anomaly map A_i is binarized into a mask M_i^j : $M_i^j = \mathbb{1}[A_i > \epsilon_j]$, where $\mathbb{1}[\cdot]$ is the indicator function. To ensure meaningful segmentation and reduce the influence of minor variations, we further apply an erosion operation to each mask M_i^j .

The third step is to find main anomaly regions that remain stable within a specific threshold range. However, the accuracy of different anomaly detection methods varies significantly, and less accurate methods may identify incorrect regions as anomalies when applying the broadest threshold range with stable segmentation, as shown in Fig. 3. To address this, we segment the dominant region stably while allowing local variations in the segmented regions with subtly threshold adjustments. Specifically, let δ_i^j denote the number of individual regions segmented in M_i^j , we first take the value that appears most frequently in $\{\delta_i^j | j \in [1, \mathcal{T}]\}$ as $\bar{\delta}_i$, which globally indicates the amount of the main regions in the anomaly map A_i . Then, to segment the main regions, we take the longest continuous threshold range where $\bar{\delta}_i$ regions are segmented consistently.

- If this range is shorter than τ , namely a manually set minimum range, it indicates that there is no anomaly region to be segmented.
- Conversely, if this range exceeds τ , it confirms stable anomaly segmentation within this threshold range. In this case, we select the minimum threshold from the identified range to segment anomalies as completely as possible.

Finally, we use the selected threshold to segment A_i into the binary mask, denoted as M_i^u . In this way, the unlabeled images set \mathcal{D}^u are extended with the binary masks: $\{(I_i^u, M_i^u) | i \in [1, N^u]\}$.

Anomaly-Centered Sub-Image Cropping. Although we minimize false positives and negatives by extracting the main abnormal regions, there might still be potential errors in the binarized masks M_i^u . To prevent their negative impact on learning, we crop each region in M_i^u individually into anomaly-centered sub-images, so that our network can pick out false-positive anomalies during learning. Specifically, for each individual region in M_i^u , we set a square box that completely encloses this region but has minimal area. Then we extend each square box by adding a 10% padding. The padding area includes the background of anomalies and thus enables our network to extract features indicating the anomaly's position on products, which is critical for classification. Notice that we keep the minimum crop size as 1% of the image size. Finally, along each square box of M_i^u , we crop a sub-image from I_i^u and its mask from M_i^u . The sub-images of I_i^u can be denoted as $\{x_{i,1}^u, x_{i,2}^u, \dots\}$, and the corresponding masks cropped from M_i^u can be denoted as $\{m_{i,1}^u, m_{i,2}^u, \dots\}$.

C. Mask-Guided Contrastive Representation Learning

This section presents Mask-Guided Contrastive Representation Learning (MGCRL). Drawing on classic NCD methods [56], [57], MGCRL engages in self-supervised learning with unlabeled data \mathcal{D}^u and labeled data \mathcal{D}^l , and supervised learning with only labeled data \mathcal{D}^l , but focusing specifically on abnormal regions. To align labeled and unlabeled inputs for MGCRL, we use the cropping method (shown in Sec. III-B) to extract sub-images and masks for the labeled data set \mathcal{D}^l , denoted as $\{(x_{i,1}^l, m_{i,1}^l), (x_{i,2}^l, m_{i,2}^l), \dots | i \in [1, N^l]\}$. These are then merged with the unlabeled data in the same structures, represented as $\{(x_{i,k}^l, m_{i,k}^l, y_{i,k}) | i \in [1, N^l + N^u], k \in [1, \bar{\delta}_i]\}$.

¹Anomaly score: Maximum value in an anomaly probability map.

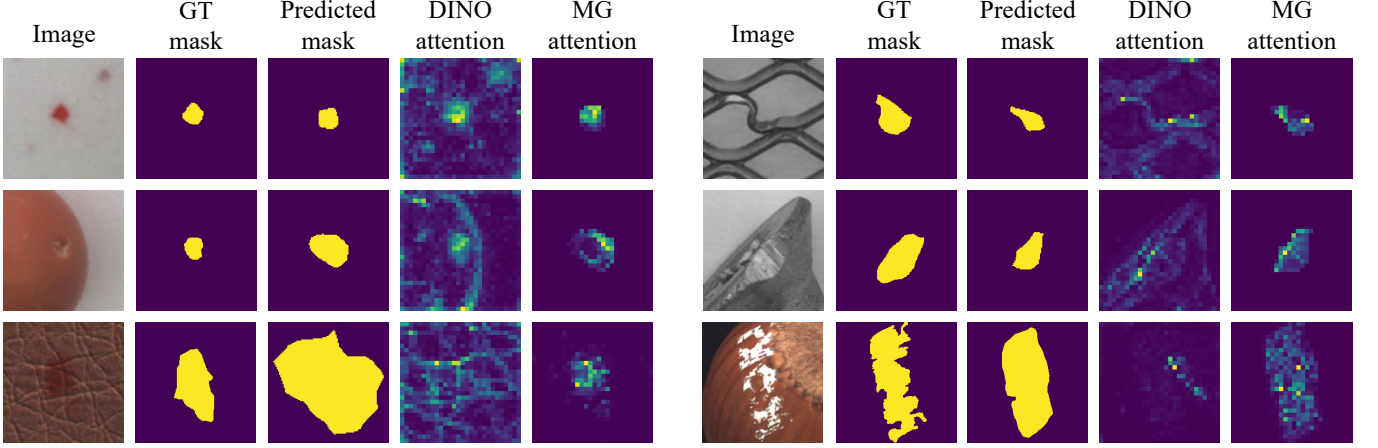


Fig. 4. **Visualization of the self-attention of the [CLS] token on the last layer’s heads.** DINO attention refers to the [CLS] token extracted from a DINO pre-trained ViT that mainly focuses on a foreground object. AnomalyNCD uses a mask to direct the [CLS] token’s attention to the anomalous regions.

where $\bar{\delta}_i$ indicates the number of sub-images per image, and $y_{i,k}$ is the anomaly category for each sub-image, matching the label of the i^{th} image if it belongs to \mathcal{D}^1 or set to -1 otherwise.

Following this, we perform the contrastive learning of [56], [57]. Firstly, each sub-image pair $(x_{i,k}, m_{i,k})$ is randomly augmented twice, generating $(\tilde{x}_{i,k}, \tilde{m}_{i,k})$ and $(\hat{x}_{i,k}, \hat{m}_{i,k})$. Then, we build two networks with the same structure (see Sec.III-C1) and shared weight but different softmax temperature settings. The “teacher” one generate pseudo label for unlabeled sub-images $\{\tilde{x}_{i,k}, \hat{x}_{i,k} | y_{i,k} = -1\}$. The “student” one is trained to classify all sub-images, as described in Sec.III-C3. During training, the pseudo labels are corrected to reduce the negative impact of normal sub-images, as shown in Sec.III-C2.

1) *Mask-Guided Vision Transformer (MGViT)*: MGViT is built on vision transformer (ViT). Thus we review its structure.

Vision transformer is a classification network that leverages the self-attention mechanism [58]. It processes an input image by dividing it into N fixed-size patches. Each patch is treated as a “token” and is flattened into an embedding vector of length D . ViT has L sequential transformer layers, each containing self-attention layers and feed-forward neural networks. In addition, a special class token, denoted as [CLS], is propagated from the first layer to the final layer where it serves as the basis for classification. In the self-attention of the l^{th} layer, the input patches undergo linear projections to form the queries, keys, and values $\mathbf{Q}_{l-1}, \mathbf{K}_{l-1}, \mathbf{V}_{l-1} \in \mathbb{R}^{(N+1) \times D}$. Here, ViT captures the relationships between the image patches by self-attention mechanism $Attn$ as follows:

$$Attn = \text{softmax}(\text{concat}(\mathbf{Q}_{l-1}^{\text{cls}} \mathbf{K}_{l-1}^{\top}, \mathbf{Q}_{l-1}^{\text{patch}} \mathbf{K}_{l-1}^{\top})) \mathbf{V}_{l-1} \quad (1)$$

where we divide \mathbf{Q}_{l-1} into $\mathbf{Q}_{l-1}^{\text{cls}} \in \mathbb{R}^{1 \times D}$ and $\mathbf{Q}_{l-1}^{\text{patch}} \in \mathbb{R}^{N \times D}$ to represent class and patch tokens separately.

Insufficient Representation for Anomalies. The ViT excels in semantic representation but fails to detect weak semantic anomalies. Fig. 4 demonstrates this using the self-attention map of the [CLS] token in the last layer of a DINO-pretrained ViT [35]. In the 1st row’s 2nd example, the model uniformly highlights the grid rather than the bent anomaly. Similarly, in the last row’s left example, it focuses on the entire texture

rather than the anomalous region. This observation means that the network over-focuses on learning background.

Mask-Guided Attention. To address the issue above, we propose the mask-guided attention to direct ViT’s focus on the anomalous region. Specifically, taking one of the augmented views $\tilde{x}_{i,k}$ as an example, it is fed into the ViT with patch amount of N . At the same time, its mask $\tilde{m}_{i,k}$ is resized to $\sqrt{N} \times \sqrt{N}$ by average pooling and then flattened into a vector $\mathcal{M} \in \mathbb{R}^{N \times 1}$. Subsequently, we insert the constant 1 at the beginning of \mathcal{M} to align its size with the tokens. Next, we use the mask vector \mathcal{M} in the self-attention mechanism for re-directing focus, which has three possible design choices.

- 1) Adding the mask \mathcal{M} on both class and patch tokens.
- 2) Adding the mask \mathcal{M} on the patch tokens.
- 3) Adding the mask \mathcal{M} on the class token.

The 1st and 2nd designs actually suppress the rich contextual features in the patch tokens that are crucial for classification, but our network only focuses on classifying anomalies rather than segmenting. Thus, the 3rd one is recommended as the most suitable design, and the experiment also verifies that our choice is effective. Such a design can be formulated as follows:

$$Attn = \text{softmax}(\text{concat}(\mathbf{Q}_{l-1}^{\text{cls}} \mathbf{K}_{l-1}^{\top} + \overline{\mathcal{M}}, \mathbf{Q}_{l-1}^{\text{patch}} \mathbf{K}_{l-1}^{\top})) \mathbf{V}_{l-1} \quad (2)$$

where $\overline{\mathcal{M}}$ denotes the converted mask vector that is compatible with the attention mechanism:

$$\overline{\mathcal{M}}(i) = \begin{cases} 0, & \text{if } \mathcal{M}(i) > 0.5 \\ -\infty, & \text{otherwise} \end{cases} \quad (3)$$

Note that, in the ViT, the self-attention in the last L_m -layer is replaced with the mask-guided attention to form MGViT. Fig. 4 reveals that the [CLS] token focuses on anomalous regions by using our mask-guided attention. Even though the predicted masks do not align with the ground truth accurately, the network still focuses on the anomaly roughly.

2) *Pseudo Labels Generation and Correction*: Based on DINO [35], we use the teacher network to generate pseudo labels for unlabeled sub-images $\tilde{x}_{i,k}, \hat{x}_{i,k}$ where $y_{i,k} = -1$. The network first computes logits $\hat{l}_{i,k} = \mathcal{H}(f(\hat{x}_{i,k}))$ and

$\tilde{l}_{i,k} = \mathcal{H}(f(\tilde{x}_{i,k}))$ in $\mathbb{R}^{C^1+C^u}$, where $f(\cdot)$ indicates MGViT that outputs the class token, and $\mathcal{H}(\cdot)$ is the linear classifier shared between teacher and student network. Note that, we set the logits in $\tilde{l}_{i,k}, \hat{l}_{i,k}$ for C^1 known classes to $-\infty$ to prevent classification into known classes. Then, a softmax with sharp temperature τ_t converts these logits $\hat{l}_{i,k}, \tilde{l}_{i,k}$ into pseudo labels $\hat{q}_{i,k}, \tilde{q}_{i,k}$. However, it has the potential to misassign pseudo-labels to over-detected regions from anomaly detection methods, which misleads multi-class classification.

To address this, we use anomaly score to correct pseudo labels, since it usually separates normal and anomaly sub-images effectively. Let $s_{i,k}$ denote the anomaly score for $x_{i,k}$, we weightedly judge whether the view $\hat{x}_{i,k}$ should be labeled as normal or assigned the generated pseudo labels.

$$\hat{q}_{i,k} \leftarrow w_{i,k} \mathbf{e}_1^{(C^u)} + (1 - w_{i,k}) \hat{q}_{i,k}; \quad w_{i,k} = \max(0.5 - s_{i,k}, 0) \quad (4)$$

where $w_{i,k}$ is the weight for normal. $\mathbf{e}_1^{(C^u)} \in \mathbb{R}^{C^u \times 1}$ denotes a unit vector whose first value is 1, in which we use the first class in the C^u classes as normal. If $s_{i,k}$ is smaller, the more likely the sub-image $\hat{x}_{i,k}$ is normal, and $\hat{q}_{i,k}$ is closer to $\mathbf{e}_1^{(C^u)}$. Thus, such correction forces the network to separate the normal sub-images from the training set. In the same way, the pseudo label $\tilde{q}_{i,k}$ is also updated.

3) *Model Training*: During training, we employ the contrastive learning that has been proven effective in [52], [56] to separate different anomalies.

- For all labeled inputs $\{\tilde{x}_{i,k}, \hat{x}_{i,k} | y_{i,k} \neq -1\}$, we simultaneously use contrastive learning [31] and supervised learning [59], which learns the knowledge of labeled anomalies and transfers it to unlabeled anomalies.
- For all unlabeled inputs $\{\tilde{x}_{i,k}, \hat{x}_{i,k} | y_{i,k} = -1\}$, we use self-supervised contrastive learning [31].

To show the training process of a mini-batch, a new subscript j is employed to replace i, k , thus the images of a batch are formed as $\{(\tilde{x}_j, \hat{x}_j)\}$, and the labels are denoted as $\{y_j\}$. Using a three-layer MLP following MGViT, denoted as $\phi(\cdot)$, we generate the logits from \tilde{x}_j and \hat{x}_j : $\tilde{z}_j = \phi(f(\tilde{x}_j))$ and $\hat{z}_j = \phi(f(\hat{x}_j))$, which are supervised by self-supervised contrastive loss:

$$\mathcal{L}_{\text{rep}}^u = \frac{1}{|B|} \sum_{j \in B} -\log \frac{\exp(\tilde{z}_j^\top \tilde{z}_j / \tau_u)}{\sum_{n \in \mathcal{N}_j} \exp(\tilde{z}_j^\top \tilde{z}_n / \tau_u)} \quad (5)$$

where B denotes a mini-batch. $|B|$ represents the number of image pairs in B . \mathcal{N}_j indexes other image pairs in the batch except (\hat{x}_j, \tilde{x}_j) , and τ_u is a temperature value. Similarly, the supervised contrastive loss for labeled data is written as:

$$\mathcal{L}_{\text{rep}}^s = \frac{1}{|B^l|} \sum_{j \in B^l} \frac{1}{|\mathcal{P}_j|} \sum_{p \in \mathcal{P}_j} -\log \frac{\exp(\tilde{z}_j^\top \tilde{z}_p / \tau_c)}{\sum_{n \in \mathcal{N}_j} \exp(\tilde{z}_j^\top \tilde{z}_n / \tau_c)} \quad (6)$$

where $B^l \subset B$ represents the indexes of labeled images in the batch B . \mathcal{P}_j indexes other images in the batch B which have the same labels as \hat{x}_j and \tilde{x}_j . τ_c is a temperature value.

For each image pair in the batch (\hat{x}_j, \tilde{x}_j) , we use the student network to generate predictions \hat{p}_j, \tilde{p}_j with a smoother temperature τ_s . For the unlabeled part $\{(\hat{x}_j, \tilde{x}_j) | y_j = -1\}$, we use the teacher network to generate pseudo labels \hat{q}_j, \tilde{q}_j with a sharper

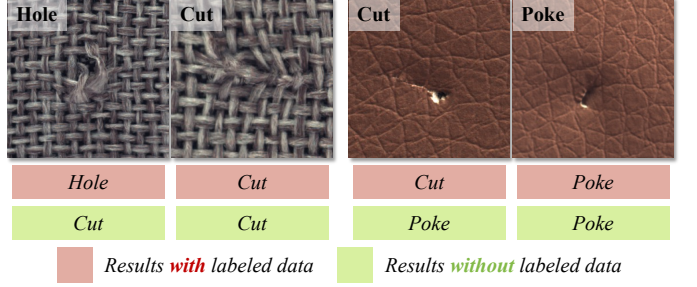


Fig. 5. **Impact of using or not using labeled data.** We show two product cases, and each presents two similar anomalies.

temperature τ_t . For the labeled part $\{(\hat{x}_j, \tilde{x}_j) | y_j \neq -1\}$, we use the ground truth as the label $\hat{y}_j = \tilde{y}_j = \text{concat}(\mathbf{e}_{y_j}^{(C^1)}, \mathbf{0}^{(C^u)})$, where $\mathbf{e}_{y_j}^{(C^1)} \in \mathbb{R}^{C^1 \times 1}$ denotes a unit vector whose y_j^{th} value is 1 and $\mathbf{0}^{(C^u)} \in \mathbb{R}^{C^u \times 1}$ denotes a zero vector.

With the representation above, we leverage the standard cross-entropy loss $\mathcal{L}_{\text{CE}}(p, q) = -\sum_{c=0}^{C^1+C^u-1} p^c \log q^c$ to optimize the classification, which is represented as:

$$\mathcal{L}_{\text{cls}}^l = \frac{1}{|B^l|} \sum_{j \in B^l} (\mathcal{L}_{\text{CE}}(\hat{y}_j, \tilde{p}_j) + \mathcal{L}_{\text{CE}}(\tilde{y}_j, \hat{p}_j)) \quad (7)$$

$$\mathcal{L}_{\text{cls}}^u = \frac{1}{|B^u|} \sum_{j \in B^u} (\mathcal{L}_{\text{CE}}(\hat{q}_j, \tilde{p}_j) + \mathcal{L}_{\text{CE}}(\tilde{q}_j, \hat{p}_j)) \quad (8)$$

where B^u indexes the unlabeled images of the batch B . Finally, we adopt a mean-entropy maximization regularizer [60] $\mathcal{L}_{\text{reg}} = \mathcal{L}_{\text{CE}}(\bar{p}_j, \bar{p}_j)$ for unlabeled sub-images, where $\bar{p}_j = \frac{1}{2|B^u|} \sum_{j \in B^u} (\hat{p}_j + \tilde{p}_j)$ denotes the mean prediction of unlabeled images. The overall loss of training objective is written as:

$$\mathcal{L} = \lambda(\mathcal{L}_{\text{rep}}^s + \mathcal{L}_{\text{cls}}^l) + (1 - \lambda)(\mathcal{L}_{\text{rep}}^u + \mathcal{L}_{\text{cls}}^u + \mu \mathcal{L}_{\text{reg}}) \quad (9)$$

where λ is a hyperparameter that balances the supervised loss and the self-supervised loss. μ is the coefficient of the regularization.

As shown in Fig. 5, labeled data is significant for MGCRL. If only using unlabeled data for contrastive learning without labeled one, MGCRL is prone to confuse anomalies with highly similar appearances. For example, a “Hole” on a carpet is treated as “Cut”, and “Cut” on leather is mis-classified as a “Poke”. Actually, even humans tend to confuse them. With the supervision of labeled data, confusion does not occur. The reason is that the labeled data helps to build the feature space of prior classes, so that even the subtle differences from novel classes can be recognized.

D. Image Classification via Region Merging Strategy

For flexible classification in both sub-image and image levels, we aim to determine the image’s anomaly class according to its sub-image classification. Intuitively, a naive method is to average the predictions of all sub-images within an image. However, false classification of the over-detected region may mislead the image class. As shown in Fig. 6, *Sub-image-1* and *Sub-image-2* are classified to *Class-2* and *Class-3*, respectively, where the wrong prediction of *Sub-image-2* misleads the image class in Fig. 6 (b).

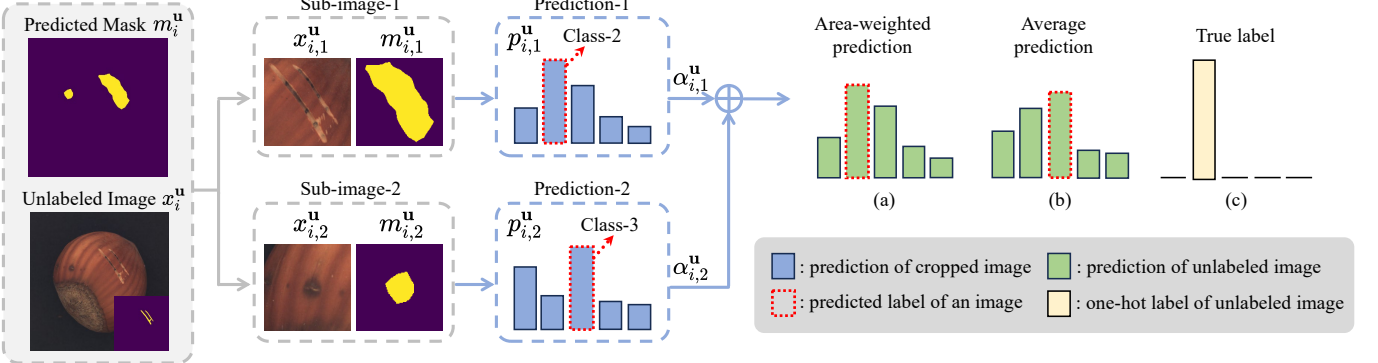


Fig. 6. **Region merging strategy for image classification.** Using average prediction, the output of normal cropped images (Sub-image-2) leads to final misclassification, while area-weighted prediction can reduce the negative effect of normal cropped images on the final result.

To address this issue, we propose a region merging approach to robustly classify images. We found that misclassification is mostly over-detected regions that are much smaller than real anomalies. Therefore, we define an area-related weight $\alpha_{i,k}^u$ for each sub-image $x_{i,k}^u$, which is used in determining the image category:

$$\alpha_{i,k}^u = \frac{\exp(\sqrt{\mathbf{a}_{i,k}^u}/\tau_\alpha)}{\sum_{k=1}^{\bar{\delta}_i} \exp(\sqrt{\mathbf{a}_{i,k}^u}/\tau_\alpha)} \quad (10)$$

where $\mathbf{a}_{i,k}^u$ is the area of anomaly in $x_{i,k}^u$, and τ_α is the temperature value. Then, for an image I_i^u composed by sub-images $\{x_{i,k}^u | k \in [1, \bar{\delta}_i]\}$, the prediction logit is $p_i^u = \sum_{k=1}^{\bar{\delta}_i} \alpha_{i,k}^u p_{i,k}^u$, where $p_{i,k}^u$ is the probability prediction of $x_{i,k}^u$ generated by the student network. As shown in Fig. 6 (a), the prediction p_i^u depends more on $p_{i,1}^u$, which has a larger weight $\alpha_{i,1}^u$ and a correct prediction.

IV. EXPERIMENTS

A. Experimental setting

1) *Datasets:* We conduct experiments on industrial datasets MVTec AD [8] and Magnetic Tile Defect (MTD) [9]. MVTec AD has industrial product images of 10 object categories and 5 texture categories. Each product category has at least two anomaly classes. Following [5] and [6], we remove the combined anomaly type for a fair comparison. Notice that our method is also capable of handling the combined anomaly type, as described in Sec. IV-C8. MTD dataset has 952 normal images and 392 abnormal images, the abnormal images are divided into five anomaly classes. We follow [5] that uses 80% of normal images as the reference images and the rest as the test images. For both datasets, we use the single-blade sub-dataset in Aero-engine Blade Anomaly Detection Dataset (AeBAD-S) [61] with the normal class removed, as our labeled abnormal image set. This dataset contains four different anomaly classes on the blade, such as breakdown, ablation, fracture, and groove.

2) *Implementation details:* We use ViT-B/8 [58] pre-trained with DINO [35] as our feature extractor. The self-attentions in the last 9 layers are replaced with our mask-guided attention. During training, all the layers of ViT are fixed except the last

layer. As with UNO[51] and BYOP[57], we use the multi-head strategy in the classifier \mathcal{H} , and use the head with the smallest loss for inference. The input images are scaled to a resolution of 224×224 . We set the batch size to 32 and epochs to 50. The Stochastic Gradient Descent (SGD) optimizer [62] is employed with a learning rate of 0.003. To generate two augmented views for contrastive learning, we follow the data augmentation strategies in BYOL [33] (random crop, flip, color jittering, and Gaussian blur) and RandAug [63] (rotation, posterize, and sharpness). Aligning with [56], the temperature values are set as follows: τ_u is 0.07 and τ_c is 1.0, τ_s is set to 0.1 and τ_t is initialized to 0.07. For the first 40 epochs, τ_t reduces every 4 epochs, linearly down to 0.04, then stays the same. For our Main Element Binarization approach, we set the \mathcal{T} to 64 and τ to 4. In the overall loss, the parameters λ and μ are respectively set to 0.3 and 4. In the Region Merging strategy, the temperature τ_α is set to 100 on the MVTec AD dataset and 50 on the MTD dataset.

For anomaly detection methods preceding AnomalyNCD, we choose zero-shot method MuSc [64], one-class methods PatchCore [54], EfficientAD [65], RD++ [66], PNI [67] and CPR [55]. Note that CPR does not provide the training code, we directly use the official checkpoints on the MVTec AD dataset. EfficientAD does not release official implementation, we use the unofficial version². For RD++ and PNI, we conduct experiments on the MTD dataset according to the configuration of MVTec AD. These unofficial results are marked in gray in Table. I.

3) *Competing methods:* We compare our method with two state-of-the-art industrial anomaly clustering methods, UniFormaly [6] and Anomaly Clustering [5] that has two settings: an unsupervised one (Unsup.) and a semi-supervised one (Semi-sup.). The former setting only input unlabeled images for clustering, while the latter one use labeled normal images, same as the input of one-class anomaly detection. We also employ three deep clustering methods, IIC [10], GATCluster [11], and SCAN [12], which cluster unlabeled images directly. In addition, four NCD methods in the nature scene are considered for comparison, UNO [51], GCD [52],

²Unofficial code for EfficientAD: <https://github.com/rximg/EfficientAD>

TABLE I
QUANTITATIVE RESULTS ON THE MVTec AD AND MTD DATASET. ALL THE METHODS USE UNLABELED IMAGES AND LABELED NORMAL IMAGES AS INPUT. THE BEST-PERFORMING RESULT IS IN BOLD. THE UNOFFICIAL RESULTS ARE MARKED IN **GRAY**.

Datasets	Metric	AC[5] (Semi-sup.)	UniFormaly[6]	PatchCore[54] +AnomalyNCD	RD++[66] +AnomalyNCD	EfficientAD[65] +AnomalyNCD	PNI[67] +AnomalyNCD	CPR[55] +AnomalyNCD
MVTec AD [8]	NMI	0.608	0.547	0.670	0.631	0.516	0.675	0.736
	ARI	0.489	0.433	0.601	0.542	0.394	0.609	0.674
	F_1	0.652	0.645	0.769	0.721	0.641	0.769	0.805
	AUPRO	-	0.953	0.938	0.950	0.917	0.942	0.964
MTD [9]	NMI	0.390	0.421	0.380	0.368	0.220	0.181	-
	ARI	0.314	0.322	0.390	0.361	0.188	0.219	-
	F_1	0.490	0.609	0.617	0.600	0.467	0.465	-
	AUPRO	-	0.837	0.729	0.741	0.731	0.516	-

TABLE II
QUANTITATIVE RESULTS ON THE MVTec AD AND MTD DATASET. ALL THE METHODS ONLY USE UNLABELED IMAGES AS INPUT. THE BEST-PERFORMING RESULT IS IN BOLD.

Datasets	Metric	IIC[10]	GATCluster[11]	SCAN[12]	UNO[51]	GCD[52]	SimGCD[56]	AMEND[68]	AC[5] (Unsup.)	MuSc [64] +AnomalyNCD
MVTec AD [8]	NMI	0.093	0.136	0.210	0.146	0.417	0.452	0.431	0.525	0.613
	ARI	0.020	0.053	0.103	0.052	0.302	0.346	0.333	0.431	0.526
	F_1	0.285	0.264	0.335	0.342	0.553	0.569	0.542	0.604	0.712
	AUPRO	-	-	-	-	-	-	-	-	0.938
MTD [9]	NMI	0.064	0.028	0.041	0.034	0.211	0.105	0.138	0.179	0.268
	ARI	0.020	0.009	0.029	0.011	0.115	0.048	0.067	0.120	0.228
	F_1	0.252	0.243	0.282	0.221	0.381	0.293	0.324	0.346	0.509
	AUPRO	-	-	-	-	-	-	-	-	0.769

SimGCD [56] and AMEND [68]. As in our method, the AeBAD-S dataset is used as labeled abnormal images.

4) *Evaluation metrics*: We report three widely used metrics for the evaluation of clustering: the F_1 score, the normalized mutual information (NMI) [69], and the adjusted rand index (ARI) [70]. We use the Hungarian algorithm [71] to match the predicted clusters to the ground truth labels. For methods using anomaly maps, we measure the segmentation per-region overlap (AUPRO) with 30% FPR [8]. All metrics are calculated by the official implementation code.

B. Quantitative results

We report the results of the multi-class anomaly classification in the MVTec AD and MTD datasets in Table I and II. All methods in Table II only use unlabeled images as input. Compared with Anomaly Clustering [5], AnomalyNCD, combined with zero-shot anomaly detection (AD) method MuSc [64], achieves 8.8% gains on NMI, 9.5% gains on ARI, and 10.8% F_1 gains, proving that AnomalyNCD extracts more discriminative features than Anomaly Clustering through contrastive learning in anomalous regions. AnomalyNCD also outperform state-of-the-art NCD methods, achieving 16.1% gains on NMI, 18.0% gains on ARI, and 14.3% F_1 gains. The performance advantage of AnomalyNCD is due to focusing on anomalies inside images.

In Table I, all methods utilize both unlabeled and labeled normal images from the same product. We integrate AnomalyNCD with various one-class AD methods. Utilizing CPR,

TABLE III
ABLATION STUDY OF DIFFERENT BINARIZATION APPROACHES ON THE MVTec AD DATASET. THE BEST-PERFORMING RESULT IS IN BOLD.

	Avg FPR \downarrow	Avg FNR \downarrow	NMI \uparrow	ARI \uparrow	F_1 \uparrow
$\epsilon = 0.1$	0.572	0.617	0.554	0.482	0.650
$\epsilon = 0.3$	0.678	0.742	0.499	0.404	0.587
$\epsilon = 0.5$	0.484	0.165	0.567	0.458	0.640
$\epsilon = 0.7$	0.269	0.247	0.495	0.395	0.623
$\epsilon = 0.9$	0.544	0.593	0.077	0.013	0.337
Otsu [72]	0.676	0.525	0.382	0.268	0.499
Ours	0.153	0.035	0.613	0.526	0.712

which achieves the highest AUPRO, leads to performance enhancements on the MVTec AD dataset: NMI increases by 10.7%, ARI by 14.9%, and F_1 score by 9.6%, surpassing other methods. On the MTD dataset, although the segmentation AUPRO of all AD methods is lower than that of UniFormaly, resulting in reduced multi-class classification performance, PatchCore+AnomalyNCD still achieves improvements of 6.8% in ARI and 0.8% in F_1 score.

C. Ablation Study

1) *Effectiveness of main element binarization*: In Table III, we report the results of using the Otsu method [72] and fixed thresholds. Since the missed detection is more critical than over-detection in industrial scenarios, we define an anomaly as detected if the intersection over union (IoU) between the actual and predicted bounding boxes exceeds 0.1. Then we

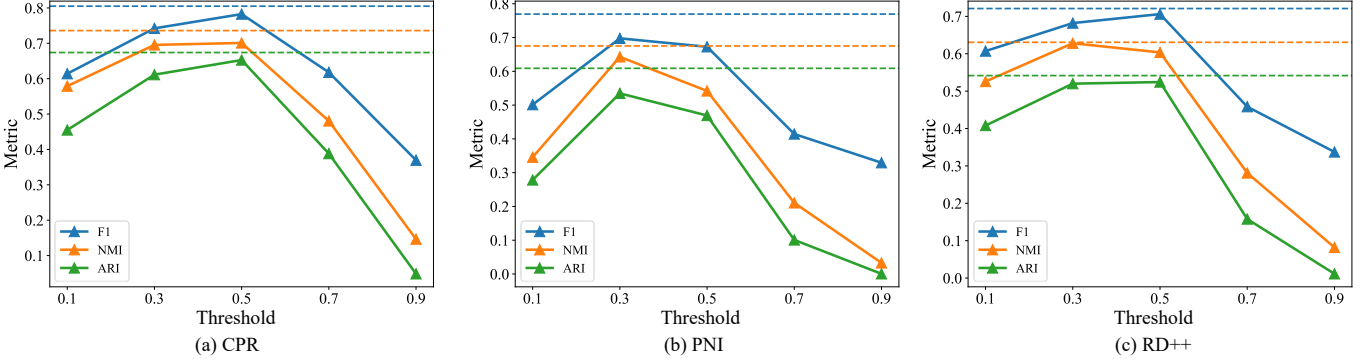


Fig. 7. The results of various anomaly detection (AD) methods under multiple fixed thresholds. The horizontal dashed line represents the results of MEBin. Notably, the optimal fixed thresholds differ across AD methods, while the model using MEBin consistently outperforms the fixed threshold results.

TABLE IV

COMPARED WITH DIFFERENT MASK ATTENTION MECHANISMS ON THE MVTec AD DATASET, THE BEST-PERFORMING RESULT IS IN BOLD.

Mask Mechanism	NMI	ARI	F_1
(a) w/o MGA	0.598	0.494	0.698
(b) mask on all tokens	0.507	0.382	0.600
(c) mask on patch tokens	0.563	0.467	0.686
(d) mask on class token (Ours)	0.613	0.526	0.712

calculate the FPR and FNR for these binarization methods. MEBin demonstrates lower FPR and FNR than fixed thresholds and Otsu, resulting in superior multi-class classification outcomes. Compared to the fixed thresholds, MEBin selects an optimal threshold for each image and achieves a 6.8% NMI improvement and a 7.2% F_1 improvement. The Otsu method tends to over-detect, particularly in normal images, making it less effective for this task.

In Fig. 7, we further apply MEBin on different one-class AD methods. These methods exhibit varying optimal fixed thresholds. For example, the optimal thresholds of CPR [55] and RD++ [66] are near 0.5, whereas for PNI [67] it is approximately 0.3. MEBin’s adaptive threshold selection consistently outperforms all fixed thresholds.

2) *Discussion of the mask-guided attention:* The mask-guided attention (MGA) makes ViT focus on tokens within the mask (anomalous region). We show the t-SNE visualization in Fig. 8. With MGA in the 3rd row, image features have larger inter-class distances (e.g. *metal_nut*) and smaller intra-class distances (e.g. *hazelnut* and *wood*) than those without MGA in the 1st row. In terms of metrics on MVTec AD, our MGA has a 1.5% NMI gain, 3.2% ARI gain, and 1.4% F_1 gain shown in Table IV.

We conduct experiments to introduce the binary mask into different tokens in Table IV. (b) introduces the binary mask on [CLS] token and all the patch tokens. (c) introduces it on all the patch tokens. Our MGA (d) only performs on [CLS] token, which is input into the classifier directly. So introducing the mask on the [CLS] token makes the classifier easier to focus on the anomaly. In addition, the context information around the anomalous region is beneficial for multi-class

TABLE V

ABLATION STUDY ON THE POSITION OF MASK-GUIDED LAYERS ON THE MVTec AD AND MTD DATASETS, THE BEST-PERFORMING RESULT IS IN BOLD.

L_m	MVTec AD			MTD		
	NMI	ARI	F_1	NMI	ARI	F_1
1	0.606	0.508	0.690	0.191	0.157	0.420
3	0.608	0.511	0.694	0.209	0.173	0.436
6	0.613	0.519	0.713	0.253	0.214	0.492
9	0.613	0.526	0.712	0.268	0.228	0.509
12	0.609	0.521	0.712	0.249	0.213	0.492

anomaly classification. We make patch tokens have a global receptive field to introduce this information indirectly into [CLS] token. Compared to other ways of introducing masks, our MGA achieves 5.0% NMI, 5.9% ARI, and 2.6% F_1 improvements.

3) *The influence of the mask-guided layer L_m :* In our method, we introduce mask-guided attention in the last L_m layers of ViT. As reported in Table V, we conduct the experiments with different mask-guided layers. The results demonstrate that using mask-guided attention in the last 9 layers yields the best performance on both datasets. When L_m is small, the [CLS] token has no chance to adequately focus on the anomaly within the binary mask. When $L_m = 12$, the [CLS] token completely lost contextual information around the anomaly, resulting in a drop in metrics. In Fig. 9, we visualize the attention maps of [CLS] tokens in different layers when $L_m = 9$. We found that the [CLS] token in layer 3 (mask-guided attention is not introduced) does not focus on the anomalous region, but on the edge with large gradient variations. When mask-guided attention is first introduced at layer 4, the entire mask region is focused. Then the attention map is gradually close to the anomaly inside the mask. In layer 12, the local anomaly can be learned well by the network.

4) *Discussion of the Anomaly-Centred Sub-Image Cropping:* The cropping operation is important for industrial anomaly clustering. The first reason is that some anomalies in industrial products are local and subtle. The cropping operation makes the anomalous region occupy most of the image, which helps the network learn the anomaly easily. As

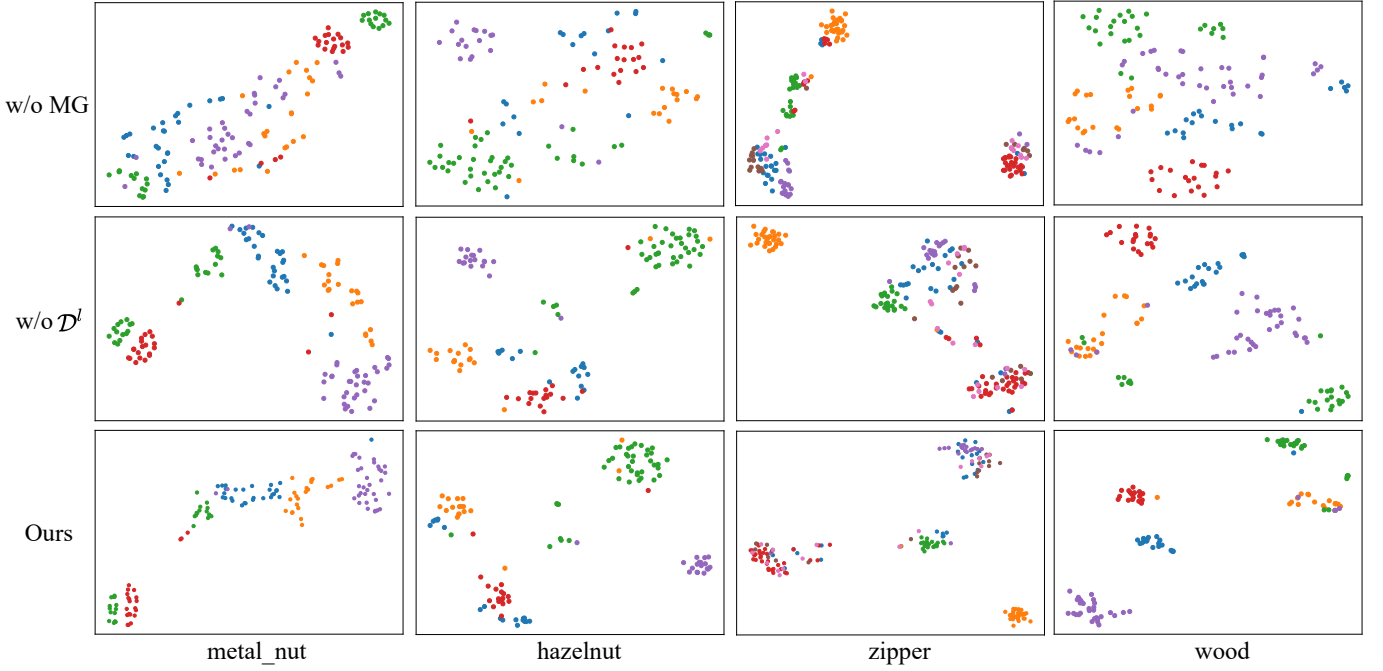


Fig. 8. T-SNE visualization of sub-images on the MVTec AD dataset. We choose *metal_nut*, *hazelnut*, *zipper* and *wood* as examples. The different colors of dots represent their anomaly classes.

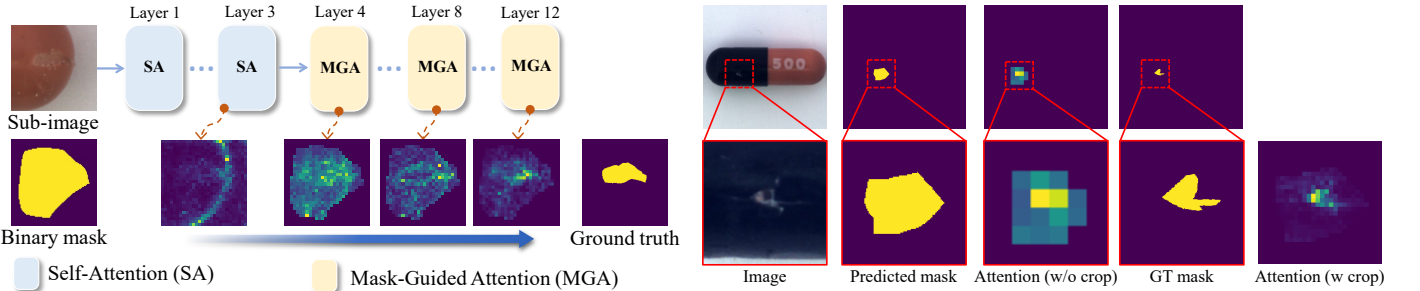


Fig. 9. Attention map of [CLS] tokens at different layers of ViT. We replace the self-attention (SA) of the last $L_m = 9$ layers with our mask-guided attention (MGA).

shown in Fig. 10, for the original image, the attention of [CLS] token has a coarse-grained response in the anomalous region. When the anomaly is subtle, the discriminative features are hard to learn. For the sub-image, the attention has a fine-grained response and learns the more discriminative pixels of subtle anomaly. We report multi-class classification on the MVTec AD and MTD datasets in Table VI. Since anomalies on the MTD dataset are subtle and finer, the crop operation is required for fine-grained feature learning, which can bring up to 23.8% NMI improvement for PatchCore+AnomalyNCD and 11.5% NMI gains for EfficientAD+AnomalyNCD. On the MVTec AD dataset, the crop operation results in a 2.0% NMI increase for PatchCore+AnomalyNCD and 1.5% NMI gain for EfficientAD+AnomalyNCD. However, when using MuSc or PNI as the anomaly detection method, it only brings a decrease in NMI of 0.9% at most.

The second reason is that the cropping operation can handle images with combined type anomalies, where there are differ-

Fig. 10. Visualization of [CLS] token's attention for entire image and sub-image.

ent types of anomalies in an image. The existing clustering methods all assume that each image has only one type of anomaly. In our method, cropping one image into sub-images can assign different labels to these sub-images. In this way, an image with combined anomalies has multi-class anomaly labels. The more details are in Sec. IV-C8.

5) *Discussion of merging strategies:* To get the classification result for an image, we need to merge the sub-image results. In Table VII, we report results using different merging strategies. (i) averaging the predictions of the sub-images, (ii) utilizing the anomaly scores of the sub-images as weights to merge, and (iii) using our region merging strategy. Strategy (iii) achieves better metrics than (i) and (ii) on both datasets. In the process of anomaly detection, there are some over-detections, which have small areas but large anomaly scores. Directly averaging results over all sub-images is inaccurate, especially when a large number of false positive sub-images are involved. Similarly, using anomaly scores as weights is also inappropriate. In contrast, our merging method, which

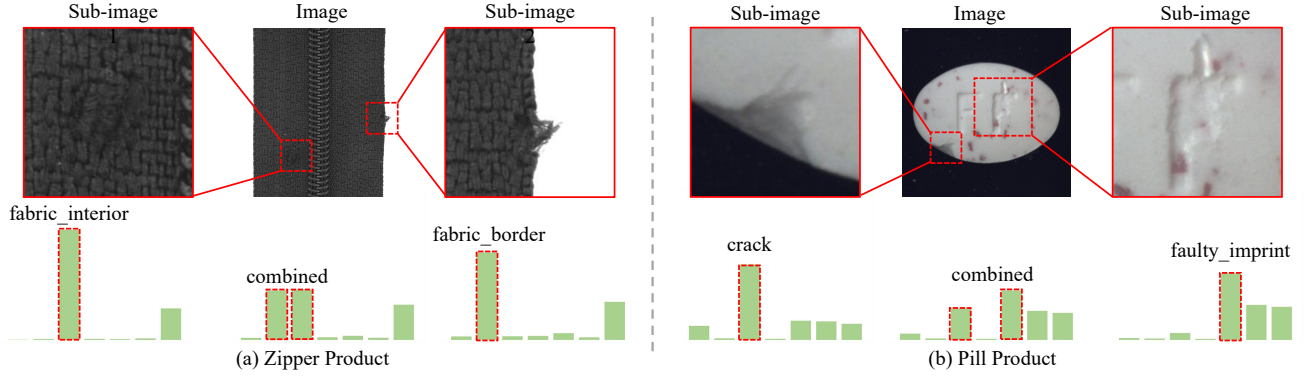


Fig. 11. **Multi-class classification results of two combined-type anomaly images.** Taking “zipper” and “pill” as examples, we show the predicted probabilities for each sub-image individually and for the entire image.

TABLE VI
ABLATION OF ANOMALY-CENTERED SUB-IMAGE CROPPING ON THE MVTec AD AND MTD DATASETS.

Dataset	Setting	MuSc[64]+AnomalyNCD			PatchCore[54]+AnomalyNCD			EfficientAD[65]+AnomalyNCD			PNI[67]+AnomalyNCD		
		NMI	ARI	F_1	NMI	ARI	F_1	NMI	ARI	F_1	NMI	ARI	F_1
MVTec AD [8]	w/o crop	0.622	0.549	0.740	0.650	0.584	0.755	0.501	0.396	0.637	0.676	0.616	0.777
	w crop	0.613	0.526	0.712	0.670	0.601	0.769	0.516	0.394	0.641	0.675	0.609	0.769
MTD [9]	w/o crop	0.086	0.076	0.374	0.142	0.166	0.432	0.105	0.066	0.379	0.107	0.134	0.407
	w crop	0.268	0.228	0.509	0.380	0.390	0.617	0.220	0.188	0.467	0.181	0.219	0.465

TABLE VII
COMPARED WITH DIFFERENT MERGING STRATEGIES ON THE MVTec AD AND MTD DATASETS.

Merge	MVTec AD			MTD		
	NMI	ARI	F_1	NMI	ARI	F_1
(i) Avg	0.610	0.521	0.709	0.257	0.223	0.501
(ii) Score Avg	0.600	0.513	0.703	0.228	0.208	0.485
(iii) Area Avg	0.613	0.526	0.712	0.268	0.228	0.509

TABLE VIII
THE ABLATION EXPERIMENT OF PSEUDO LABEL RE-CORRECTION (PLR) ON THE MVTec AD DATASET. WE EVALUATE THE PRECISION AND RECALL OF THE NORMAL CLASS.

	Precision	Recall	NMI	ARI	F_1
w/o PLR	0.797	0.727	0.597	0.517	0.714
w PLR	0.821	0.876	0.613	0.526	0.712

assigns weights to multiple sub-image predictions based on area, has more robust merged predictions compared to these two strategies.

6) *Effect of Pseudo Label Re-correcting:* Our Pseudo Label Re-correcting (PLR) aims to reduce the impact of sub-images with over-detections. The over-detected sub-images are part of the normal images and have large appearance differences, which makes it difficult to correctly group them into the same normal class. In Table VIII, we report the precision and recall of the normal class. After performing PLR, the recall achieves 14.9% improvements, which means that some normal sub-images are misclassified before, and the PLR corrects these sub-images into normal class. An improvement of 1.6% NMI

TABLE IX
THE ABLATION EXPERIMENT OF USING LABELED ABNORMAL IMAGES \mathcal{D}^1 ON THE MVTec AD AND MTD DATASETS.

	MVTec AD			MTD		
	NMI	ARI	F_1	NMI	ARI	F_1
w/o \mathcal{D}^1	0.583	0.506	0.689	0.227	0.202	0.485
w \mathcal{D}^1	0.613	0.526	0.712	0.268	0.228	0.509

is reflected in the multi-class classification results.

7) *Discussion of the labeled abnormal images:* In the labeled abnormal images \mathcal{D}^1 , there is much prior knowledge of industrial anomalies classification, such as anomalies with similar size, color, and location belonging to the same class. Using them to train the network together can transfer the knowledge from \mathcal{D}^1 to the network and separate confusing anomalies from each other in \mathcal{D}^u . As shown in Fig. 8, we use the AeBAD-S dataset [61] as \mathcal{D}^1 in the last row, but not in the second row. When labeled abnormal images are used, the image features extracted from ViT have larger inter-class distances (e.g. *leather*) and smaller intra-class distances (e.g. *wood*). We report the quantitative results in Table IX, using \mathcal{D}^1 brings 3.0% NMI improvements on MVTec AD and 3.9 % NMI improvements on MTD.

8) *Discussion on how to handle the combined category:* In Table II, we follow AC [5] to remove the combined class for a fair comparison. However, the combined class is quite common in the industrial scene, such as the *cable*, *pill*, *wood*, and *zipper* products on the MVTec AD dataset. The image with the combined class contains multiple different types of anomalies, yet current clustering methods can only classify

TABLE X

THE QUANTITATIVE RESULTS OF USING THE GROUND TRUTH MASKS. WE COMPARE OUR ANOMALY NCD WITH ANOMALY CLUSTERING ON THE MVTec AD AND MTD DATASETS.

Methods	MVTec AD			MTD		
	NMI	ARI	F_1	NMI	ARI	F_1
AC [5]	0.711	0.638	0.718	0.467	0.359	0.482
Ours	0.871	0.851	0.909	0.829	0.863	0.841

the entire image into one anomaly type. For our method, we crop the image into many sub-images, and each sub-image is assigned a label by the classifier. In this way, all the anomalous regions in the combined image can be found and classified individually. As shown in Fig. 11, there are two types of anomalies in the zipper and pill products respectively. Each anomalous region is cropped and correctly classified. By merging the prediction of the sub-images to the entire image, we find that classifying the image as these two types of anomalies has a higher probability.

9) *The results of using ground truth masks:* In the previous section, we demonstrated that our multi-class classification performs better when the anomaly detection method performs better. So in order to test the optimal results of our AnomalyNCD, we assume an ideal anomaly detection method where the ground truth mask of the unlabeled image is available. We report the results in Table X, our approach achieves significant improvement over anomaly clustering on two datasets. On MVTec AD, there is a 16.0% improvement on the NMI and a 19.1% improvement on the F_1 , and on MTD, there is a 36.2% improvement on the NMI and a 35.9% improvement on the F_1 . In this ideal case, ground truth masks do not introduce any over-detections and missed detections compared to anomaly maps generated by anomaly detection methods. With the improvement of anomaly detection methods in the future, our AnomalyNCD can achieve better results.

V. CONCLUSION

In this paper, we focus on the problem of recognizing visual classes of industrial anomalies. We propose AnomalyNCD, a multi-class anomaly classification framework for industrial vision, which is compatible with existing anomaly detection methods. To isolate the over-detection and missed detection brought by anomaly detection methods, we first propose the main element binarization approach, which roughly extracts the anomalous regions and then crops each anomalous region into sub-images. We then leverage mask-guided contrastive representation learning to direct the network focus on the anomalous regions and learn discriminative representations. Finally, our region merging strategy achieves flexible classification at sub-image and image levels during inference. Extensive experiment results on the MVTec AD and MTD datasets demonstrate the effectiveness of our framework.

A. Acknowledgments

This work was supported by the National Natural Science Foundation of China under Grant No.62176098. The computa-

tion is completed in the HPC Platform of Huazhong University of Science and Technology.

REFERENCES

- [1] J. Jeong, Y. Zou, T. Kim, D. Zhang, A. Ravichandran, and O. Dabir, “Winclip: Zero-/few-shot anomaly classification and segmentation,” in *IEEE Conf. Comput. Vis. Pattern Recog.*, 2023, pp. 19 606–19 616.
- [2] Y. Liang, J. Zhang, S. Zhao, R. Wu, Y. Liu, and S. Pan, “Omni-frequency channel-selection representations for unsupervised anomaly detection,” *IEEE Trans. Image Process. (TIP)*, vol. 32, pp. 4327–4340, 2023.
- [3] B. Hu, B. Gao, W. L. Woo, L. Ruan, J. Jin, Y. Yang, and Y. Yu, “A lightweight spatial and temporal multi-feature fusion network for defect detection,” *IEEE Trans. Image Process. (TIP)*, vol. 30, pp. 472–486, 2021.
- [4] Z. Zeng, B. Liu, J. Fu, and H. Chao, “Reference-based defect detection network,” *IEEE Trans. Image Process. (TIP)*, vol. 30, pp. 6637–6647, 2021.
- [5] K. Sohn, J. Yoon, C.-L. Li, C.-Y. Lee, and T. Pfister, “Anomaly clustering: Grouping images into coherent clusters of anomaly types,” in *Winter Conf. Appl. Comput. Vis.*, 2023, pp. 5479–5490.
- [6] Y. Lee, H. Lim, S. Jang, and H. Yoon, “Uniformaly: Towards task-agnostic unified framework for visual anomaly detection,” *arXiv preprint arXiv:2307.12540*, 2023.
- [7] K. Han, A. Vedaldi, and A. Zisserman, “Learning to discover novel visual categories via deep transfer clustering,” in *Int. Conf. Comput. Vis.*, 2019, pp. 8401–8409.
- [8] P. Bergmann, M. Fauser, D. Sattlegger, and C. Steger, “Mvtac ad—a comprehensive real-world dataset for unsupervised anomaly detection,” in *IEEE Conf. Comput. Vis. Pattern Recog.*, 2019, pp. 9592–9600.
- [9] Y. Huang, C. Qiu, and K. Yuan, “Surface defect saliency of magnetic tile,” *Vis. Comput.*, vol. 36, pp. 85–96, 2020.
- [10] X. Ji, J. F. Henriques, and A. Vedaldi, “Invariant information clustering for unsupervised image classification and segmentation,” in *IEEE Conf. Comput. Vis. Pattern Recog.*, 2019, pp. 9865–9874.
- [11] C. Niu, J. Zhang, G. Wang, and J. Liang, “Gatcluster: Self-supervised gaussian-attention network for image clustering,” in *Eur. Conf. Comput. Vis.*, 2020, pp. 735–751.
- [12] W. Van Gansbeke, S. Vandenhende, S. Georgoulis, M. Proesmans, and L. Van Gool, “Scan: Learning to classify images without labels,” in *Eur. Conf. Comput. Vis.*, 2020, pp. 268–285.
- [13] Y. Yan, H. Hao, B. Xu, J. Zhao, and F. Shen, “Image clustering via deep embedded dimensionality reduction and probability-based triplet loss,” *IEEE Trans. Image Process. (TIP)*, vol. 29, pp. 5652–5661, 2020.
- [14] J. Lv, Z. Kang, X. Lu, and Z. Xu, “Pseudo-supervised deep subspace clustering,” *IEEE Trans. Image Process. (TIP)*, vol. 30, pp. 5252–5263, 2021.
- [15] C. Niu, H. Shan, and G. Wang, “Spice: Semantic pseudo-labeling for image clustering,” *IEEE Trans. Image Process. (TIP)*, vol. 31, pp. 7264–7278, 2022.
- [16] Y.-C. Hsu, Z. Lv, and Z. Kira, “Learning to cluster in order to transfer across domains and tasks,” in *Int. Conf. Learn. Represent.*, 2018.
- [17] Y.-C. Hsu, Z. Lv, J. Schlosser, P. Odom, and Z. Kira, “Multi-class classification without multi-class labels,” in *Int. Conf. Learn. Represent.*, 2019.
- [18] K. Han, S.-A. Rebuffi, S. Ehrhardt, A. Vedaldi, and A. Zisserman, “Autonovel: Automatically discovering and learning novel visual categories,” *IEEE Trans. Pattern Anal. Mach. Intell.*, vol. 44, no. 10, pp. 6767–6781, 2021.
- [19] Z. Zhong, L. Zhu, Z. Luo, S. Li, Y. Yang, and N. Sebe, “Openmix: Reviving known knowledge for discovering novel visual categories in an open world,” in *IEEE Conf. Comput. Vis. Pattern Recog.*, 2021, pp. 9462–9470.
- [20] S. Vaze, A. Vedaldi, and A. Zisserman, “No representation rules them all in category discovery,” *Adv. Neural Inform. Process. Syst.*, vol. 36, 2023.
- [21] J. Fan, D. Liu, H. Chang, H. Huang, M. Chen, and W. Cai, “Seeing unseen: Discover novel biomedical concepts via geometry-constrained probabilistic modeling,” *IEEE Conf. Comput. Vis. Pattern Recog.*, 2024.
- [22] J. Zhou, Y. Liu, and Q. Chen, “Novel class discovery in chest x-rays via paired images and text,” in *AAAI Conf. Artif. Intell.*, vol. 38, no. 7, 2024, pp. 7650–7658.
- [23] W. Liang, F. Xue, Y. Liu, G. Zhong, and A. Ming, “Unknown sniffer for object detection: Don’t turn a blind eye to unknown objects,” in *IEEE/CVF Conference on Computer Vision and Pattern Recognition*, 2023.

[24] Z. Liu, X. Zhao, T. Huang, R. Hu, Y. Zhou, and X. Bai, “TANet: Robust 3D Object Detection from Point Clouds with Triple Attention,” in *AAAI Conf. Artif. Intell.*, 2020.

[25] J. Ma, A. Ming, Z. Huang, X. Wang, and Y. Zhou, “Object-level proposals,” in *IEEE International Conference on Computer Vision (ICCV)*, 2017.

[26] A. Ming, T. Wu, J. Ma, F. Sun, and Y. Zhou, “Monocular depth-ordering reasoning with occlusion edge detection and couple layers inference,” in *IEEE Intelligent Systems (IS)*, vol. 31, no. 2, 2016, pp. 54–65.

[27] A. Ming, B. Xun, J. Ni, M. Gao, and Y. Zhou, “Learning discriminative occlusion feature for depth ordering inference on monocular image,” in *IEEE International Conference on Image Processing (ICIP)*, 2015.

[28] R. Lu, F. Xue, M. Zhou, A. Ming, and Y. Zhou, “Occlusion-shared and feature-separated network for occlusion relationship reasoning,” in *IEEE/CVF International Conference on Computer Vision (ICCV)*, 2019.

[29] Y. Zhou, R. Lu, F. Xue, and Y. Gao, “Occlusion relationship reasoning with a feature separation and interaction network,” *Visual Intelligence*, vol. 1, no. 1, p. 23, 2023.

[30] K. He, H. Fan, Y. Wu, S. Xie, and R. Girshick, “Momentum contrast for unsupervised visual representation learning,” in *IEEE Conf. Comput. Vis. Pattern Recog.*, 2020, pp. 9729–9738.

[31] T. Chen, S. Kornblith, M. Norouzi, and G. Hinton, “A simple framework for contrastive learning of visual representations,” in *Int. Conf. Mach. Learn.*, 2020, pp. 1597–1607.

[32] A. v. d. Oord, Y. Li, and O. Vinyals, “Representation learning with contrastive predictive coding,” *arXiv preprint arXiv:1807.03748*, 2018.

[33] J.-B. Grill, F. Strub, F. Altché, C. Tallec, P. Richemond, E. Buchatskaya, C. Doersch, B. Avila Pires, Z. Guo, M. Gheshlaghi Azar *et al.*, “Bootstrap your own latent-a new approach to self-supervised learning,” *Adv. Neural Inform. Process. Syst.*, vol. 33, pp. 21271–21284, 2020.

[34] X. Chen and K. He, “Exploring simple siamese representation learning,” in *IEEE Conf. Comput. Vis. Pattern Recog.*, 2021, pp. 15 750–15 758.

[35] M. Caron, H. Touvron, I. Misra, H. Jégou, J. Mairal, P. Bojanowski, and A. Joulin, “Emerging properties in self-supervised vision transformers,” in *Int. Conf. Comput. Vis.*, 2021, pp. 9650–9660.

[36] Q. Xie, M.-T. Luong, E. Hovy, and Q. V. Le, “Self-training with noisy student improves imagenet classification,” in *IEEE Conf. Comput. Vis. Pattern Recog.*, 2020, pp. 10 687–10 698.

[37] S. Gong, H. Zhou, F. Xue, C. Fang, Y. Li, and Y. Zhou, “Fastroadseg: Fast monocular road segmentation network,” *IEEE Trans. Intell. Transp. Syst.*, vol. 23, no. 11, pp. 21 505–21 514, 2022.

[38] Y. Chang, F. Xue, F. Sheng, W. Liang, and A. Ming, “Fast road segmentation via uncertainty-aware symmetric network,” in *IEEE Int. Conf. Robot. Automat.*, 2022, pp. 11 124–11 130.

[39] H. Zhou, F. Xue, Y. Li, S. Gong, Y. Li, and Y. Zhou, “Exploiting low-level representations for ultra-fast road segmentation,” *IEEE Transactions on Intelligent Transportation Systems*, pp. 1–11, 2024.

[40] S. Bhownik, R. Sarkar, B. Das, and D. Doermann, “GiB: A Game Theory Inspired Binarization Technique for Degraded Document Images,” *IEEE Trans. Image Process. (TIP)*, vol. 28, no. 3, pp. 1443–1455, 2019.

[41] Y. E. Salehani, E. Arabnejad, A. Rahiche, A. Bakhta, and M. Cheriet, “MSdBNMF: Multispectral document image binarization framework via non-negative matrix factorization approach,” *IEEE Trans. Image Process. (TIP)*, vol. 29, pp. 9099–9112, 2020.

[42] K. Nitirogiannis, B. Gatos, and I. Pratikakis, “Performance evaluation methodology for historical document image binarization,” *IEEE Trans. Image Process. (TIP)*, vol. 22, no. 2, pp. 595–609, 2013.

[43] T. Sund and K. Eilertsen, “An algorithm for fast adaptive image binarization with applications in radiotherapy imaging,” *IEEE Trans. Med. Imaging*, vol. 22, no. 1, pp. 22–28, 2003.

[44] S. Roy, A. Dey, K. Chatterjee, and S. K. Bandyopadhyay, “A new efficient binarization method for mri of brain image,” *Signal, Image Process.*, vol. 3, no. 6, p. 35, 2012.

[45] F. Xue, A. Ming, and Y. Zhou, “Tiny obstacle discovery by occlusion-aware multilayer regression,” *IEEE Trans. Image Process. (TIP)*, vol. 29, pp. 9373–9386, 2020.

[46] F. Xue, A. Ming, M. Zhou, and Y. Zhou, “A novel multi-layer framework for tiny obstacle discovery,” in *IEEE Int. Conf. Robot. Automat.*, 2019.

[47] F. Xue, Y. Chang, T. Wang, Y. Zhou, and A. Ming, “Indoor obstacle discovery on reflective ground via monocular camera,” *Int. J. Comput. Vis.*, vol. 132, no. 3, pp. 987–1007, 2024.

[48] B. Su, S. Lu, and C. L. Tan, “Robust document image binarization technique for degraded document images,” *IEEE Trans. Image Process. (TIP)*, vol. 22, no. 4, pp. 1408–1417, 2012.

[49] W. Wu, Y. Zhao, M. Z. Shou, H. Zhou, and C. Shen, “Diffumask: Synthesizing images with pixel-level annotations for semantic segmentation using diffusion models,” in *Int. Conf. Comput. Vis.*, 2023, pp. 1206–1217.

[50] J. Ahn and S. Kwak, “Learning pixel-level semantic affinity with image-level supervision for weakly supervised semantic segmentation,” in *IEEE Conf. Comput. Vis. Pattern Recog.*, 2018, pp. 4981–4990.

[51] E. Fini, E. Sangineto, S. Lathuiliere, Z. Zhong, M. Nabi, and E. Ricci, “A unified objective for novel class discovery,” in *Int. Conf. Comput. Vis.*, 2021, pp. 9284–9292.

[52] S. Vaze, K. Han, A. Vedaldi, and A. Zisserman, “Generalized category discovery,” in *IEEE Conf. Comput. Vis. Pattern Recog.*, 2022, pp. 7492–7501.

[53] P. Gu, C. Zhang, R. Xu, and X. He, “Class-relation knowledge distillation for novel class discovery,” in *Int. Conf. Comput. Vis.*, 2023, pp. 16 428–16 437.

[54] K. Roth, L. Pemula, J. Zepeda, B. Schölkopf, T. Brox, and P. Gehler, “Towards total recall in industrial anomaly detection,” in *IEEE Conf. Comput. Vis. Pattern Recog.*, 2022, pp. 14 318–14 328.

[55] H. Li, J. Hu, B. Li, H. Chen, Y. Zheng, and C. Shen, “Target before shooting: Accurate anomaly detection and localization under one millisecond via cascade patch retrieval,” *arXiv preprint arXiv:2308.06748*, 2023.

[56] X. Wen, B. Zhao, and X. Qi, “Parametric classification for generalized category discovery: A baseline study,” in *IEEE Conf. Comput. Vis. Pattern Recog.*, 2023, pp. 16 590–16 600.

[57] M. Yang, L. Wang, C. Deng, and H. Zhang, “Bootstrap your own prior: Towards distribution-agnostic novel class discovery,” in *IEEE Conf. Comput. Vis. Pattern Recog.*, 2023, pp. 3459–3468.

[58] A. Dosovitskiy, L. Beyer, A. Kolesnikov, D. Weissenborn, X. Zhai, T. Unterthiner, M. Dehghani, M. Minderer, G. Heigold, S. Gelly *et al.*, “An image is worth 16x16 words: Transformers for image recognition at scale,” in *IEEE Conf. Comput. Vis. Pattern Recog.*, 2021.

[59] P. Khosla, P. Teterwak, C. Wang, A. Sarna, Y. Tian, P. Isola, A. Maschinot, C. Liu, and D. Krishnan, “Supervised contrastive learning,” *Adv. Neural Inform. Process. Syst.*, vol. 33, pp. 18 661–18 673, 2020.

[60] M. Caron, I. Misra, J. Mairal, P. Goyal, P. Bojanowski, and A. Joulin, “Unsupervised learning of visual features by contrasting cluster assignments,” *Adv. Neural Inform. Process. Syst.*, vol. 33, pp. 9912–9924, 2020.

[61] Z. Zhang, Z. Zhao, X. Zhang, C. Sun, and X. Chen, “Industrial anomaly detection with domain shift: A real-world dataset and masked multi-scale reconstruction,” *Comput. Ind.*, vol. 151, p. 103990, 2023.

[62] L. Bottou, “Large-scale machine learning with stochastic gradient descent,” in *Int. Conf. Comput. Statist.*, 2010, pp. 177–186.

[63] E. D. Cubuk, B. Zoph, J. Shlens, and Q. V. Le, “RandAugment: Practical automated data augmentation with a reduced search space,” in *IEEE Conf. Comput. Vis. Pattern Recog. Worksh.*, 2020, pp. 702–703.

[64] X. Li, Z. Huang, F. Xue, and Y. Zhou, “Musc: Zero-shot industrial anomaly classification and segmentation with mutual scoring of the unlabeled images,” in *Int. Conf. Learn. Represent.*, 2024.

[65] K. Batzner, L. Heckler, and R. König, “Efficientad: Accurate visual anomaly detection at millisecond-level latencies,” in *Proceedings of the IEEE/CVF Winter Conference on Applications of Computer Vision*, 2024, pp. 128–138.

[66] T. D. Tien, A. T. Nguyen, N. H. Tran, T. D. Huy, S. Duong, C. D. T. Nguyen, and S. Q. Truong, “Revisiting reverse distillation for anomaly detection,” in *IEEE Conf. Comput. Vis. Pattern Recog.*, 2023, pp. 24 511–24 520.

[67] J. Bae, J.-H. Lee, and S. Kim, “Pni: industrial anomaly detection using position and neighborhood information,” in *Int. Conf. Comput. Vis.*, 2023, pp. 6373–6383.

[68] A. Banerjee, L. S. Kallooriyakath, and S. Biswas, “Amend: Adaptive margin and expanded neighborhood for efficient generalized category discovery,” in *Winter Conf. Appl. Comput. Vis.*, 2024, pp. 2101–2110.

[69] C. D. Manning, *An introduction to information retrieval*, 2009.

[70] W. M. Rand, “Objective criteria for the evaluation of clustering methods,” *J. Am. Stat. Assoc.*, vol. 66, no. 336, pp. 846–850, 1971.

[71] H. W. Kuhn, “The hungarian method for the assignment problem,” *Nav. Res. Logist. Q.*, vol. 2, no. 1-2, pp. 83–97, 1955.

[72] N. Otsu, “A threshold selection method from gray-level histograms,” *IEEE Trans. Syst. Man Cybern.*, vol. 9, no. 1, pp. 62–66, 1979.